# Outdoor sound propagation modeling in realistic environments: Application of coupled parabolic and atmospheric models

Bertrand Lihoreau, Benoit Gauvreau,[a] and Michel Bérengier
*Laboratoire Central des Ponts et Chaussées, Section Acoustique Routière et Urbaine, B.P. 4129, 44341 Bouguenais cedex, France*

Philippe Blanc-Benon
*Laboratoire de Mécanique des Fluides et d'Acoustique de I'Ecole Centrale de Lyon, UMR CNRS 5509, 69314 Ecully Cedex, France*

Isabelle Calmet
*Laboratoire de Mécanique des Fluides de I'Ecole Centrale de Nantes, UMR CNRS 6598, B.P. 92101, 44321 Nantes cedex 03, France*

(Received 11 March 2005; revised 14 April 2006; accepted 21 April 2006)

Predicting long-range sound propagation over a nonurban site with complex propagation media requires the knowledge of micrometeorological fields in the lower part of the atmospheric boundary layer, and more precisely its characteristics varying in both space and time with respect to local ("small-scale") and average ("long-term") conditions, respectively. Thus in this study, a mean-wind wide-angle parabolic equation (MW-WAPE) code is coupled with a dedicated micrometeorological code (SUBMESO) which simulates wind and temperature fields over moderately complex terrain with high resolution. Its output data are used as input data for the MW-WAPE code, which can also deal with different boundary conditions, such as the introduction of impedance jumps, thin screens or complex topography. Both codes are presented in the present paper. Comparisons between numerical predictions, and experimental data are also presented and discussed. Finally, we present an example of such a coupling method (MW-WAPE/SUBMESO) for the estimation of sound pressure levels at almost any site ("local scale"), for mean propagation conditions representative of long-term atmospheric conditions. 
[DOI: 10.1121/1.2204455]

PACS number(s): 43.28.Js, 43.50.Vt, 43.28.En, 43.28.Gq [DKW] Pages: 110–119

## I. INTRODUCTION

In the framework of road traffic noise characterization and particularly for engineering applications (impact studies), there is a need for reliable sound pressure level (SPL) predictions for specific source-receiver configuration and propagation conditions, which must be representative of time ("long term") and space ("small scale" and site effects) characteristics of the acoustic situation. This is carried out in the present study, using a coupling approach with reference models for both acoustic and micrometeorological calculations. This paper focuses on this coupling method, which can give us access to SPL fluctuations due to both time and space variations of input data. Our micrometeorological code can use large-scale input data which can be chosen as representative of long-term (several years average) meteorological data, leading to small-scale (or "local-scale") output data, representative of long-term micrometeorological conditions at a considered site. At last, those data are used as input data for the acoustic model, leading to SPL predictions for small-scale *and* long-term representative propagation conditions.

Predicting long-range sound propagation over a nonurban site implies taking into account the mixed influence of ground characteristics (topography, obstacles, impedance, etc.) and atmospheric conditions (refraction and turbulence). These phenomena have been separately studied in the literature.[1] In recent years, several authors have developed numerical simulations of sound propagation in the atmosphere taking into account atmospheric models. To model sound propagation in the atmospheric boundary layer, the basic idea recently introduced is to use a mesoscale atmospheric model to simulate local wind and temperature profiles in an area above a terrain having a complex topography. This atmospheric model is coupled with an appropriate model for sound propagation. A first approach has been considered by Heimann and Gross[2] to simulate the temporal behavior of the sound pressure level across a narrow valley. In their work, a numerical sound particle model based on ray-tracing technique is coupled with a meteorological mesoscale model. Hole and Hauge[3] successfully applied the coupling method to describe the influence on sound propagation on a local scale of a morning air temperature inversion above a complex terrain. In their numerical simulations, the authors used a mesoscale atmospheric model (MM5) to provide input data for their acoustical predicting model based on a fast field program. In this model, the local sound speed in each vertical layer is calculated as the sum of the adiabatic sound speed and the wind component in the direction of the acoustic wave propagation. Recently, a different

[a]Author to whom correspondence should be addressed; electronic mail: benoit.gauvreau@lcpc.fr

approach has been considered to improve the modeling of sound propagation in an inhomogeneous moving atmosphere. These new numerical simulations are based on time-domain calculations performed with linearized equations of fluid dynamics.[4–6] The interest in these finite-difference time-domain techniques is their ability to deal with complicated phenomena in outdoor sound propagation, such as scattering by turbulence, three-dimensional (3D) effects by buildings, and topography. However, a high computational effort is necessary to run these solvers, and this approach is not yet appropriate to deal with long-range sound propagation problems.

The numerical predictions from our parabolic equation (PE) code have been previously quantitatively compared to numerical, analytical, and experimental results already published for gradually more complex situations: homogeneous, heterogeneous, and/or screened ground,[7,8] homogeneous, stratified, and/or turbulent atmosphere.[9,10] Concerning uneven ground, the model has been validated through a comparison with results obtained from a method using conformal mapping.[11,12] Comparative results show very good agreement for frequencies from 100 Hz to 5000 Hz.[13–15] Before presenting new computing results from our mean-wind wide-angle PE (MW-WAPE) code, this acoustic code is briefly presented in Sec. II. Numerical simulations have been developed using the paraxial approximation of the wave equation in bidimensional configurations with a split-step Padé marching algorithm. Afterward, PE predictions are compared to outdoor measurements especially carried out at the Laboratoire Central des Ponts et Chaussées (LCPC) experimental site (Sec. III). Comparative results for different geometrical configurations and atmospheric conditions are presented and discussed. Some improvements are obtained using the MW-WAPE instead of the classical PE (WAPE) regarding the convection effect of the wind on SPL.

Since wind and temperature profiles are required as input data for the acoustic code, they can be either experimentally determined or numerically synthesized by a micrometeorological model suited to the study of atmospheric flows at submesoscales and is called SUBMESO. This atmospheric model is presented in Sec. II B. It is a 3D nonhydrostatic compressible model derived from the advanced regional prediction system (ARPS) model.[16] The predictions are performed using large-eddy simulation (LES), which gives access to all 3D wind components as well as air temperature at each point of the mesh (50 m $\times$ 50 m) for different heights. Comparisons between SUBMESO predictions and micrometeorological data from the LCPC experimental site are shown and discussed in the next section. Finally, output data from SUBMESO is used as input data for PE predictions, leading to a coupling method (MW-WAPE/SUBMESO) to estimate the long-term SPL at a fixed site. An example of such a coupling approach is presented and discussed in Sec. IV.

## II. THEORETICAL BACKGROUND

The principle of our coupling approach is to use *reference models* (i.e., reliable and validated models) for acoustic and micrometeorological calculations, in order to have access to reliable SPL predictions for a given situation in space (local scale) and time (long term). Thus, synthetic temperature and wind fields from SUBMESO are used as input data for PE calculations. In this section, we briefly present the MW-WAPE and SUBMESO codes, respectively.

### A. Parabolic equation

The PE-based methods seem to be appropriate to solve the problem of acoustic propagation above a mixed ground with topographical irregularities in a refractive and turbulent atmosphere (see Sec. I). For numerical simulations of outdoor sound propagation, PEs have been derived using the approximation of the effective sound speed to take into account the convection effect of the wind. In this conventional approach, the real moving atmosphere is replaced by hypothetical motionless medium with the effective sound speed $c_{\text{eff}}=c+v_x$, where $v_x$ is the wind velocity component along the direction of sound propagation between the source and receiver, and $c$ is the adiabatic sound speed. This approach is convenient because both the source and receiver are close to the ground and the preferred direction of sound is nearly horizontal. However, in many problems of atmospheric acoustics, refracted sound waves propagate in directions which may significantly differ from the direction of propagation.[17–19] We use a specific PE developed by Ostashev *et al.*[20] and Dallois *et al.*[21] which does maintain the vector properties of the velocity medium. We consider bidimensional $(x,z)$ propagation of a monochromatic acoustic wave in a homogeneous and moving medium. If the length scale of the medium $L$ is much greater than the acoustic length scale, $\lambda \ll L$, an exact wave equation for this situation in the frequency domain is given by Ostashev *et al.*:[20]

$$\left[\Delta + k^2(1+\epsilon) - \sqrt{1+\epsilon}\frac{2ik}{c} v\cdot\nabla + \frac{v_x v_z}{c^2}\frac{\partial^2}{\partial_x \partial_z}\right] p(r) = 0, \quad (1)$$

where $p$ is the acoustic pressure, $k=\omega/c$, $c$ is the sound speed, $\omega=2\pi f$, $f$ is the frequency, $\epsilon=(c_0/c(r))^2-1$ is the variation of the standard refraction index, $c_0$ is a reference sound speed, $x$ and $z$ are, respectively, the horizontal and vertical directions, and $v$ stands for the velocity of the medium. When $v=0$, Eq. (1) is reduced to the Helmholtz equation:

$$[\Delta + k_0^2(1+\epsilon)]p(r) = 0. \quad (2)$$

The additional terms in Eq. (1), compared to Eq. (2), contain the effects of the moving medium. Ostashev *et al.*[20] and Dallois *et al.*[21] reduced Eq. (1) to WAPE. The first step is to write the two-dimensional equation for forward propagation:

$$\left[\frac{\partial}{\partial x} - ik\sqrt{Q}\right] p(r) = 0. \quad (3)$$

From here, the pseudo-operator $\sqrt{Q}$ is simplified using a Padé approximation to yield:

$$\sqrt{Q} = \frac{1+pL}{1+qL}, \quad (4)$$

where $L=Q-1$, $p=3/4$, and $q=1/4$. Considering the envelope of the pressure field defined as $\phi(r)=p(r)\exp(-ik_x)$, the

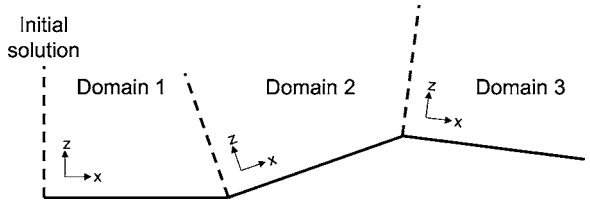


FIG. 1. Definition of the computational domains.

parabolic equation transforms to the MW-WAPE:

$$[1+qF_1-ipkM_1-qk^2M_1^2]\frac{\partial\phi}{\partial_x}=ik[(p-q)F_1 + ik(p-q)M_1-ikM_1F_1+qk^2M_1^2]\phi, \tag{5}$$

where

$$F_1=\frac{1}{c^2-v_x^2}\left[c_0^2+2ic_0\frac{v_z}{k}\frac{\partial}{\partial z}+\frac{c^2-v_z^2}{k^2}\frac{\partial^2}{\partial z^2}\right]-1,$$

and

$$M_1=\frac{2v_x}{k(c^2-v_x^2)}\left[ic_0-\frac{v_z}{k}\frac{\partial}{\partial z}\right].$$

If all velocities in Eq. (5) are set to zero, this equation is reduced to the classical Padé (1.1) WAPE derived from the Helmholtz equation [Eq. (2)]:

$$[I+qL]\frac{\partial\phi(r)}{\partial x}=ik_0[(p-q)L]\phi(r), \tag{6}$$

where

$$L=\varepsilon_{\text{eff}}+\frac{1}{k}\frac{\partial^2}{\partial z^2}, \tag{7}$$

with

$$\varepsilon_{\text{eff}}=n_{\text{eff}}^2-1=c_0^2/c_{\text{eff}}^2-1. \tag{8}$$

Equations (3) and (5) are discretized on a uniform mesh $(i\Delta x, j\Delta z)$ using a standard finite difference method. Vertical $(z-)$ derivatives are evaluated by centered difference approximations, and Crank-Nicholson scheme is implemented as a marching algorithm which takes the following form:

$$A\phi(x+\Delta x,z)=B\phi(x,z), \tag{9}$$

where $A$ and $B$ are pentadiagonal (MW-WAPE) or trigonal (WAPE) matrices. In our computations, the ground is modeled as a locally reacting surface with finite complex impedances calculated using the one parameter approximation from Delany and Bazley.[22] (see Sec. IV). Reflections at the top of the numerical grid are controlled by introducing a thin artificial absorption layer in the upper part of the computation domain.

The uneven ground is treated as a succession of flat domains.[11–15] After each flat domain, the coordinate system $(x,z)$ is rotated so that the $x$-axis remains parallel to the ground (Fig. 1). The calculation above each domain needs an initial solution. The values of the initial solution for the domain $n+1$ are obtained from the interpolated values of the pressure field of the domain $n$, except for the first domain where the source is initialized by a Gaussian starter which has an adjustable width and takes into account the image source weighed by a complex reflection coefficient.

There are several ways of modeling the vertical wind and temperature, profiles near the ground: Linear, logarithmic, multilinear, linear logarithmic, hybrid, etc. As first-order approximations, temperature and wind profiles are set constant with distance (nonrange dependent) on each flat domain. Likewise, the profiles, are slightly rotated with each corresponding domain, since the angles between the rotated systems of coordinates are very small (inferior to 5°). Moreover, following Panofsky and Dutton[23] and Gilbert and White,[24] vertical temperature and wind profiles are assumed to be logarithmically shaped and expressed, respectively, as:

$$T(z)=T(z_0+d)+a_T\ln\left(\frac{z-d}{z_0}\right)\ (\text{K}),$$
$$v(z)=a_v\ln\left(\frac{z-d}{z_0}\right)\ (\text{m/s}), \tag{10}$$

where $d$ is the displacement length, $z_0$ is the roughness parameter, and $a_T$ and $a_v$ are refraction parameters related to temperature and wind, respectively. The effective sound speed $c_{\text{eff}}$ used in the classical Padé (1,1) PE [Eq. (6)] is defined from wind and temperature fields as:

$$c_{\text{eff}}(z)=c_0\sqrt{1+\frac{T(z)}{273.15}}+v(z)\cos(\theta)\ (\text{m/s}), \tag{11}$$

and next:

$$c_{\text{eff}}(z)\approx c_0\left(1+\frac{1}{2}\frac{T_0}{273.15}\right)+\left(\frac{1}{2}\frac{c_0}{273.15}a_T+\cos(\theta)a_v\right)\times\ln\left(\frac{z-d}{z_0}\right)\ (\text{m/s}), \tag{12}$$

where $T_0$(K) is a reference temperature (e.g., $T_0=293.15$ K), $c_0$ (m/s) is a reference sound speed for the same temperature (e.g., $c_0\approx 344$ m/s for $T_0=293.15$ K), and $\theta$ is the angle between wind direction and the direction of sound propagation. We can define an effective refraction parameter $a_{\text{eff}}$ as follows:

$$a_{\text{eff}}=\frac{1}{2}\frac{c_0}{273.15}a_T+\cos(\theta)a_v\ (\text{m/s}). \tag{13}$$

This effective refraction parameter is used with WAPE while temperature and wind refraction parameters are used with MW-WAPE. In this paper, atmospheric turbulence is not considered. However, MW-WAPE can deal: with isotropic and homogeneous turbulence (only due to temperature fluctuations), where the random temperature field is modeled by a set of realizations (typically 50 realizations) which are generated by a superposition of discrete random Fourier modes.[25]

### B. Atmospheric model

Our MW-WAPE code needs accurate propagation conditions as input data for calculations. Vertical sound speed

profiles are determined from wind and temperature profiles through Eq. (10) after data postprocessing. Those profiles can be also numerically synthesized by a micrometeorological model. This is carried out in the following section using an atmospheric code, called SUBMESO, whose theory is presented below. Next, the code is validated through comparison with experimental data from LCPC monitoring site located at Saint-Berthevin (France).

In this study, all the simulations are performed with the SUBMESO atmospheric model, which is derived from the ARPS.[16] It is a nonhydrostatic compressible model suited to the study of atmospheric flows at submesoscales. The equations are written in the so-called Gal-Chen, or terrain-following coordinate system. An option for the stretching of the mesh in the vertical $z$ direction is available, while the grid needs to be regularly spaced in the horizontal $x$ and $y$ directions. The equations are discretized on the staggered grid of a Cartesian computational domain and are then transformed in the physical domain by means of the Jacobian method. Second-order accurate finite difference schemes are used to evaluate the derivatives. The solution is advanced in time using a time-splitting method[26] where all the terms in governing equations are computed explicitly. The simulations are performed using the LES method, which gives access to instantaneous fields. The flow is initialized using analytical profiles built with a meteorological preprocessor, the parameters of which are deduced from measurements: Roughness length, velocity friction, surface heat fluxes, etc. From these profiles, one can deduce the corresponding values of large-scale wind (at the highest level) that are constant during the simulation in the Rayleigh damping layer. The periodic computation on the flat coarse grid provides time-dependent turbulent inflow at the boundaries of the uneven nested grids. The subgrid fluxes are evaluated according to the Smagorinsky's model[27] modified by Lilly.[28]

The accuracy of the solution obtained by resolving the discrete Navier-Stokes equations depends directly on the mesh size. Because of the numerous time and space scales involved in the evolution of atmospheric flows, local refinement techniques are of great interest for meteorological simulations. The refinement technique used in this study is the nesting method in the horizontal direction, which consists in superposing fine grids covering small areas on a coarse grid covering the whole domain. The nesting procedure is managed as externally as possible—that is without modifying the core of the code—by means of the technical module adaptative grid refinement in FORTRAN (AGRIF) which was coupled to the atmospheric model.[29,30] Although the AGRIF module is designed to manage adaptive nesting, only fixed nested grids, are used in this study to achieve high resolution in the vicinity of particular sites. Particular care was given to the formulation of the nested grid boundary conditions, which should avoid spurious noise at the interface. Here, boundary points where the flow is entering—"inflow" boundary—are distinguished from boundary points where the flow is exiting—"outflow" boundary. At inflow boundaries, information should naturally arrive from outside, that is, from the coarse grid: The boundary values are specified through a Dirichlet-type condition. At outflow boundaries, the flow is mostly determined from the inner part of the fine grid and should be able to pass freely across the interface without boundary reflection. The method retained for outflow boundaries is the "radiative-nesting condition" applied to the velocity components and to the temperature while a Dirichlet condition is used for pressure.[31–33]

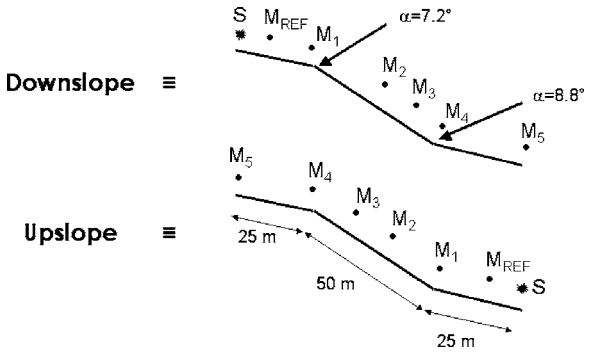


FIG. 2. Schematic illustration of the experimental setup at LCPC experimental site.

## III. QUANTITATIVE RESULTS FROM MW-WAPE PREDICTIONS

A dedicated experimental campaign has been carried out at the LCPC monitoring site near Saint-Berthevin, whose protocol is briefly presented below. New results from comparison with MW-WAPE predictions are next discussed, focusing on the influence of the following parameters: Wind speed and direction, slope of the terrain, and receiver height.

### A. Experimental setup

This specific campaign has been carried out on the most complex part of the LCPC experimental site: Uneven ground and very heterogeneous ground impedance.[13] For the calculations, the ground is modeled as a succession of three flat domains (Fig. 2): The first is 25 m long and has a slope of 10.21°, the second is 50 m long and has a slope of 17.42°, and the third is 25 m long and has a slope of 8.61°. The relative angle between the first and the second domain is $\alpha = 7.2°$ and $\alpha = 8.8°$ between the second and the third domain. Acoustic data have been collected using an impulsive and omnidirectional sound source (gun shots) and five microphones spatially distributed between 25 and 100 m from the source (M1 to M5 in Fig. 2). The reference microphone was located 10 m from the source ($M_{ref}$).

The ground impedance $Z$ has been experimentally determined at several points through a "best-fit" calculation using the one-parameter formula from Delany and Bazley:[22]

$$Z = \rho_0 c_0 \left( 1 + 0.0571 \left( \frac{\rho_0 f}{\sigma} \right)^{-0.754} + i 0.087 \left( \frac{\rho_0 f}{\sigma} \right)^{-0.732} \right), \tag{14}$$

where $c_0$ is the reference sound speed, $\rho_0$ is the air density, and $\sigma$ is the airflow resistivity. The parameter $\sigma$ is experimentally determined using a method developed by Bérengier *et al.*[34] The results of the fitting procedures for downslope propagation are (see Fig. 2): $\sigma = 600$ kPa s m$^{-2}$ around the

TABLE I. Micrometeorological parameters deduced from experimental data: $\theta$ is the angle between wind direction and the direction of sound propagation, $a_T$ and $a_v$ are refraction parameters related to temperature and wind respectively, and $a_{\text{eff}}$ is the effective refraction parameter (see Sec. II A).

| Measurement | $a_v$(m/s) | $\theta$(°) | $a_T$(K) | $a_{\text{eff}}$ (m/s) |
|---|---|---|---|---|
| **4** | 0.30 | 60 | 0.20 | 0.27 |
| **7** | 0.65 | 20 | 0.20 | 0.73 |
| **9** | 0.30 | 70 | 0.30 | 0.28 |
| **11** | 0.00 | ··· | −0.30 | −0.18 |

source, $\sigma=90$ kPa s m$^{-2}$ around M1, $\sigma=160$ kPa s m$^{-2}$ around M2, and $\sigma=200$ kPa s m$^{-2}$ around M4.

In order to evaluate the micrometeorological conditions, we used an equipped tower located on the slope but far enough from the measurement line not to disturb acoustic propagation. The tower is equipped with ventilated air thermometers; (Young 41342VC) and accurate wind direction and wind speed sensors (Young 05305AQ), using a Young 26700 station, the accuracy is about 0.1 K, 2°, and 0.1 m/s respectively. The sampling rates of the temperature and wind measurements are too low as to derive turbulence parameters. These sensors are located at three different heights: 1, 3, and 10 m. Temperature and wind profiles are modeled following Eq. (10), where $a_T$ and $a_v$ are deduced from micrometeorological measurements (10 min average). For each acoustical measurement, the signal has been averaged over ten gun shots, which is a sufficient number to determine a reliable average value for acoustical measurements.[35] Results are given in terms of relative SPL coming from the difference between the spectrum at microphone M1, M2, M3, M4, or M5 and the spectrum at the reference microphone $M_{\text{ref}}$. Tables I and II, respectively, summarize micrometeorological and geometrical parameters deduced from data postprocessing, and used as input data for PE calculations.

### B. Comparison between experimental results and numerical predictions

Figure 3 shows results from Measurement No. 7 performed for downslope propagation and for $h_s=h_M=h_{\text{ref}}=2m$ (see Table II). The corresponding micrometeorological parameters are summarized in Table I. The wind is moderately strong and almost directed in the source-receiver direction, which leads to a downward refracting atmosphere. Therefore, Fig. 3 allows us to compare acoustic results, either experimental (solid line) or calculated with the standard PE (WAPE – dotted line) and with the new PE (MW-WAPE – dashed line).

TABLE II. Geometrical parameters of experimental setup and numerical predictions: Source height $h_s$, reference receiver height $h_{\text{ref}}$, and microphone height $h_{\text{M}}$ (see Sec. III A).

| Measurement No. | Slope | $h_s$(m) | $h_{\text{ref}}$(m) | $h_{\text{M}}$(m) |
|---|---|---|---|---|
| **4** | Down | 2 | 2 | 2 |
| **7** | Down | 2 | 2 | 2 |
| **9** | Down | 2 | 0.6 | 0.6 |
| **11** | Up | 2 | 2 | 2 |

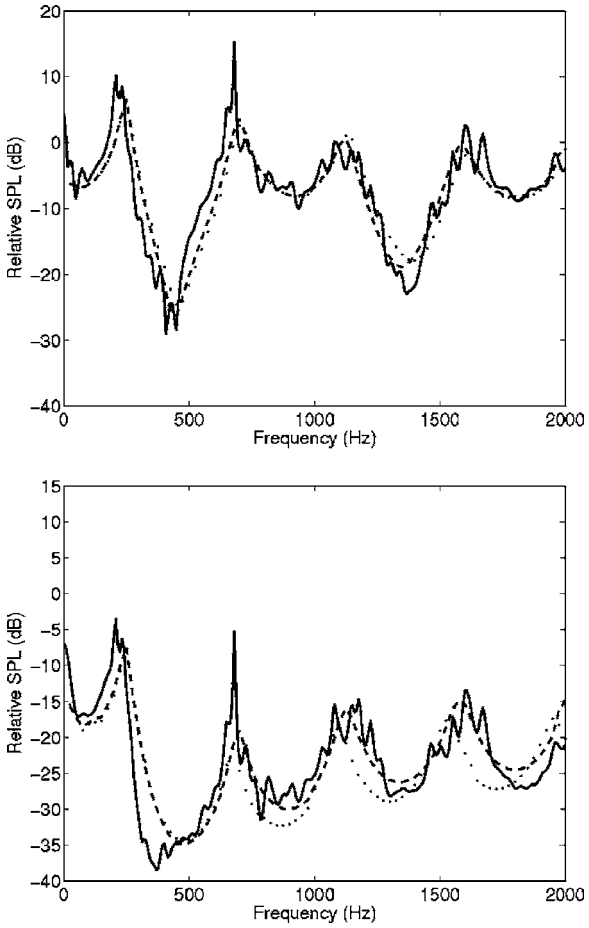


FIG. 3. Measurement No. 7. Relative SPL as a function of frequency: Comparison between experimental results (solid line) and PE predictions (WAPE in dotted line and MW-WAPE in dashed line). (a) M1 (25 m) and (b) M4 (75 m).

Numerical predictions are in very good agreement with experimental data, especially those given by the new PE (MW-WAPE), which gives a best localization of interference fringes for highest frequencies. This difference increases with the distance of propagation. In terms of geometric acoustics, this means that the receiver can be reached following two different paths: A direct and a reflected ray. The sound speed $(c+v\cos\theta)$ varies on each ray with $\theta$, and the use of the effective sound speed $(c+v_x)$ introduces a cumulative phase error in standard parabolic equation. This error increases with receiver height, distance of propagation, and wind speed.

Additional calculations for different geometrical configurations, slopes, and atmospheric conditions have confirmed that there is no significant difference between the results from WAPE and MW-WAPE when the wind is very low. On the contrary, as far as the wind is moderately strong, cross-wind effects are always better taken into account using new MW-WAPE instead of standard WAPE. From now on, the numerical results further presented in this paper will be issued from the MW-WAPE code. Above 2000 Hz, wavelength and ground roughness are of the same order. This

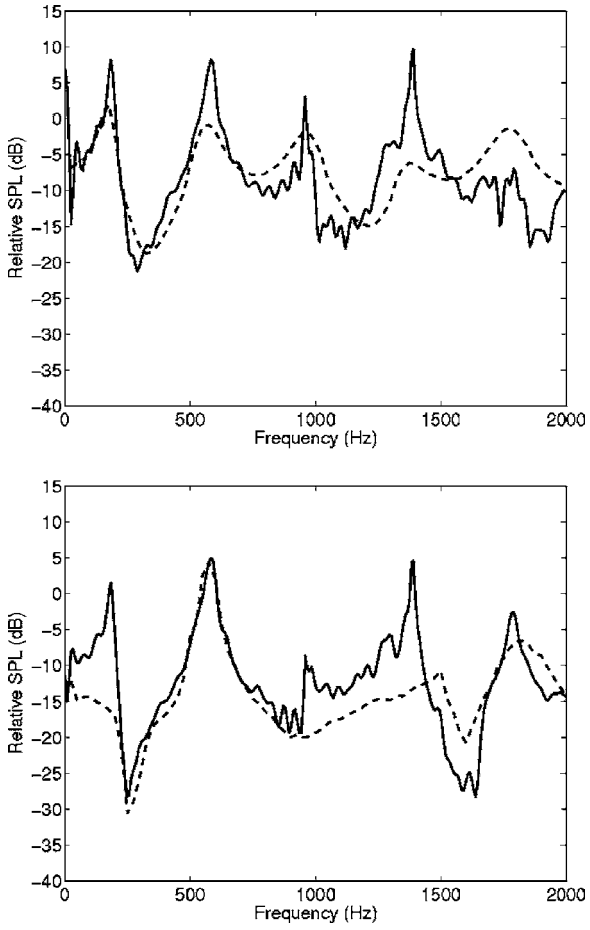


FIG. 4. Measurement No. 11. Relative SPL as a function of frequency: Comparison between experimental results (solid line) and MW-WAPE predictions (dashed line). (a) M1 (25 m) and (b) M4 (75 m).

leads to an additional diffraction which is not modeled by the acoustic code. That is the reason why comparative results above 2000 Hz are not presented. Regarding acoustic propagation for upslope cases, Fig. 4 shows results, from Measurement No. 11 ($h_s=h_{\mathrm{ref}}=h_{\mathrm{M}}=2m$, see Table II). The propagation conditions are slightly upward refracting (see Table I).

Numerical results show very good agreement with the experimental results at frequencies below 1000 Hz. Above 1000 Hz, numerical predictions are not as close to the experimental data. These discrepancies come from different causes. First, particular attention has to be paid to the numerical models sensibility, with respect to the spatial location of source and receivers ($h_s$, $h_{\mathrm{ref}}$, and $h_{\mathrm{M}}$, see Sec. III A), which can generate large uncertainties in MW-WAPE predictions when a lack of precision occurs in the *in situ* measurement of those geometrical input data. Second, the experimental terrain is more irregular on the bottom than on the top of the site. Thus, it is possible that discrepancies between numerical and experimental approaches result from 3D effects. Third, the Delany and Bazley's approach [Eq. (14)] gives good approximations, but remains limited. A more complex model of the ground, such as Attenborough's,[36] should improve our PE predictions. This model includes, more physical factors: Air flow resistivity $\sigma$, porosity $\Omega$, grain shape factor $n'$, and pore shape factor ratio $s_f$. Nevertheless, its implementation remains difficult because these

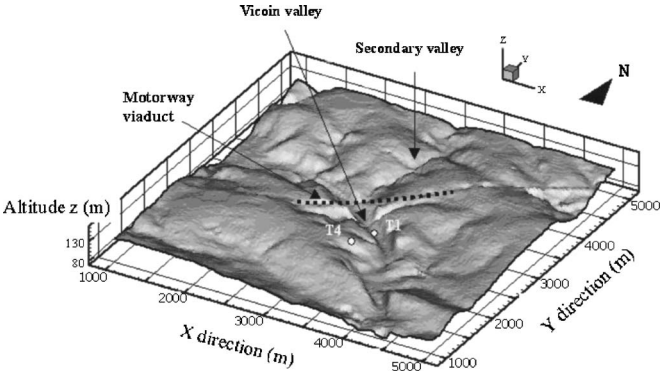


FIG. 5. Topography of the LCPC experimental site located at Saint-Berthevin. The resolution is 25 m. The vertical direction is stretched by a factor of 5 in order to make the topography more noticeable.

four factors ($\sigma$, $\Omega$, $n'$, and $s_f$) cannot be easily characterized by *in situ* measurements. Last, but not least, the differences between experimental and numerical SPL for the highest frequencies (above 1000 Hz) can also be explained by the effects of atmospheric turbulence,[37–41] which have not been taken into account in those MW-WAPE calculations for central processing unit time reasons.

## IV. PRACTICAL EXAMPLES OF MW-WAPE/SUBMESO COUPLING

This section shows how SUBMESO gives us access to synthetic local (site-scale) wind and temperature vertical profiles from global ones (regional scale), which can be chosen next as representative values of "long-term" (e.g., a 30 years average) atmospheric conditions. Those last conditions are given by national meteorological stations (Météo-France, for instance), which record hourly data over dozens of years. Thus, SUBMESO can provide wind and temperature profiles for the characterization of a specific situation both in *space* (local scale) and *time* (long term). Then, output data from SUBMESO can be used as micrometerological input data for PE calculations between the source and receiver. Therefore, our MW-WAPE/SUBMESO coupling method can provide SPL representative of *local* and *long-term* atmospheric conditions between the source and receiver. This procedure is briefly presented below, before showing some calculations from the coupled MW-WAPE/SUBMESO code.

LES of the atmospheric flow above the LCPC experimental site located at Saint-Berthevin have been performed to assess the terrain-induced modifications of the mean flow and turbulence characteristics over hilly surfaces. This study is part of a research plan directed by the LCPC for controlling long-range noise pollution in the surroundings of motorways.

The studied area is centered on the permanent source of noise pollution, which is a motorway viaduct crossing the valley of the river Vicoin. This valley, which has an approximately average depth of 35 m and an average width of 200 m, crosses the domain from north-west to south-east. A tributary stream coming from the north in a smaller valley joins the river Vicoin near the center of the site. The smooth topography of the 16 km$^2$ area is displayed in Fig. 5, based

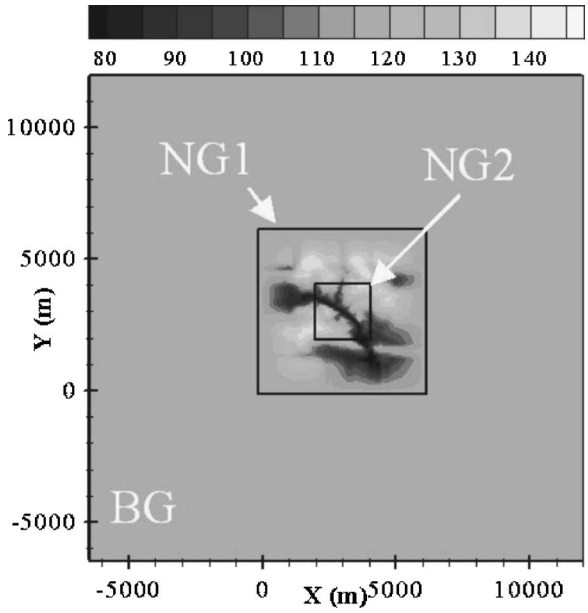


FIG. 6. BG (flat) and the two nested grids NG1 and NG2 (with topography), for the site of Saint-Berthevin.

on a digital terrain model (DTM) with a resolution of 25 m provided by the French National Geographical Institute (IGN). Total relief amplitude is 67 m ranging from 73 m in the lower part of the valley (near the south boundary) to 140 m at the northern edge of the domain.

Three levels of grids are used, which are displayed in Fig. 6. At the first level, a base grid (BG) has a horizontal resolution of 450 m with $43\times43$ points (18.9 km $\times$18.9 km). The terrain is flat and its altitude is set to the terrain average altitude $z_a=115.2$ m. At the second level, the nested grid (NG1) has a horizontal resolution of 150 m, with $44\times44$ points. The domain covered by this grid (6.15 km $\times$6.15 km) includes the whole 16 km$^2$ area defined in DTM. The area is extended in the horizontal directions so that the terrain is flat at the boundaries of NG1, insuring a proper connection at the BG/NG1 interface at the altitude $z_a$. Finally, a third grid (NG2) is nested into the grid NG1, centred on the motorway viaduct. It has a horizontal resolution of 50 m, with $44\times44$ points (2.15 km$\times$2.15 km). Note that the topography on the grid NG2 is thus more detailed than on the grid NG1. For the three grids, 32 layers are distributed in the vertical direction, following a geometric series (with a common ratio of 1.2). The thinnest mesh layer is 10 m deep, at the ground. A Rayleigh damping layer extends from $z=4000$ m to the top of the domain (7500 m). Periodic conditions are imposed at the boundaries of the BG, providing time-dependent turbulent inflow at the boundaries of the uneven area NG1.

A period of neutral atmospheric stratification (i.e., without thermal effects)—May 21, from 1:45 to 3:15—was selected among the data available from the experimental campaign conducted in May 2000. Initially, a uniform wind profile is set in the larger domain and the flow is forced by a constant large-scale wind ($U=3.3$ m/s in the west-east direction and $V=2.7$ m/s in the south-north direction). The initial wind direction is 230° clockwise from the north.

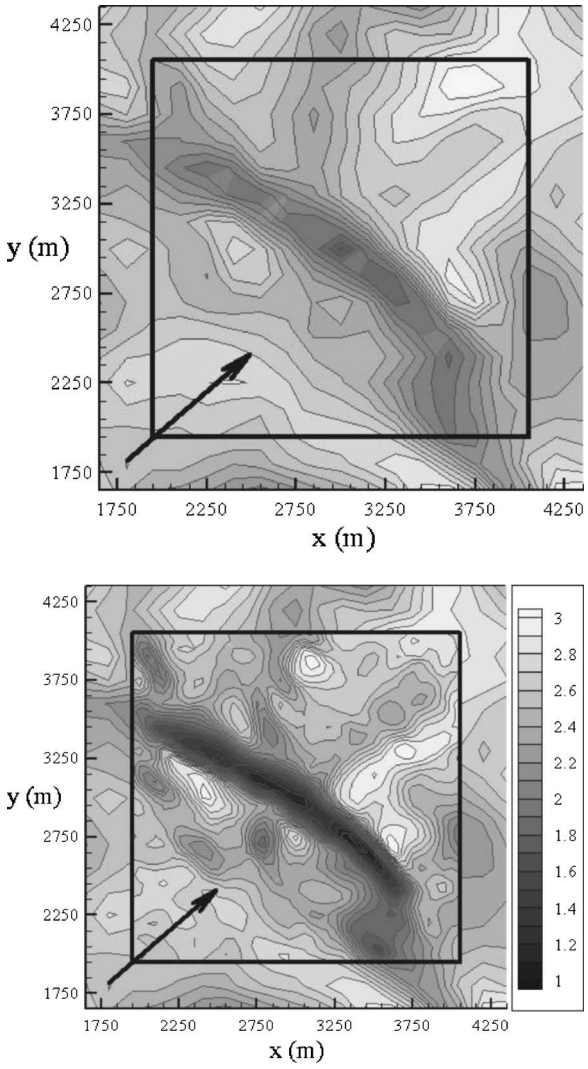


FIG. 7. Partial $x$-$y$ view of the simulated wind field $W_1$ (m/s) at Saint-Berthevin, at the first grid level (5 m) above the ground (a) on NG1 (the black square represents the location of NG2) and (b) on NG2 overlapping NG1. The black arrow symbolizes the mean wind direction.

The surface temperature is uniform at the ground and kept constant during the whole simulation. As a first approach, the air is considered to be dry. After 1400 s, the wind profile calculated on NG2 locally matches quite well with the experimental profile measured at the tower (T4) (see Fig. 5 for the location of this tower). A time average is calculated between $t=1400$ s and $t=1500$ s with an output time step of 1 s for NG2. From this procedure, we get smoothed local fields hereafter designated by the index I. We compare these fields with their value averaged over the entire domain, hereafter designated by the index m. In the following discussion, we pay a particular attention to the deformation of the total wind.

The first important result is the improved quality of the simulated flow provided by the grid refinement technique. This conclusion is obvious from Fig. 7, which displays the simulated wind field at 5 m above the ground on both NG1 and NG2. The main features—slowdown and speedup effects in valleys and over hills—are visible at both resolution levels, but they are strongly diffused and smoothed on NG1. In

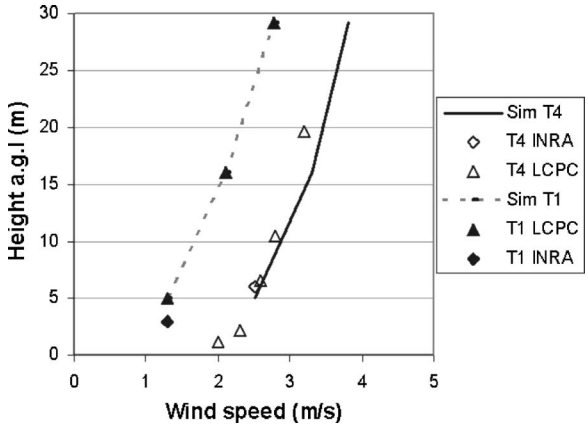


FIG. 8. Wind vertical profiles at Saint-Berthevin, from measurements ("T4/T1 INRA", "T4/T1 LCPC") and from simulation ("Sim T4" and "Sim T1"), at two locations T4 (3050 m, 2650 m) and T1 (3150 m, 2900 m). Note that the ground level is not the same for T1 to T4.

particular, we notice a great difference in the estimation of the slowdown in the Vicoin valley, which is nearly perpendicular to the mean wind direction: With a 50 m resolution, the wind speed is found to be reduced of up to 58% compared to its mean value $W_m$, whereas it is reduced of a maximum of 31% only with a 150 m resolution.

These differences can be explained by two factors. First, the highest resolution on NG2 naturally restrains the numerical diffusion of the solution. Second, the terrain features are much more accurately described on NG2 than on NG1, for which the topography is artificially smoothed. It is interesting to note that the value of the mean wind $W_m$ on NG2 is between 2 and 3% lower than the value on NG1 in the first 300 m above the ground. This is probably due to more accurate calculation of the valley-induced deceleration when the horizontal resolution is improved from 150 m to 50 m.

The second important result is the absence of significant perturbations at the NG1/NG2 interface. The wind field is continuous from one grid to the other at inflow boundaries, as imposed by the Dirichlet-type condition. At outflow boundaries, we can naturally see slight "jumps" from NG2 to NG1 as the solution is less forced, but no induced numerical oscillations are visible. The radiative-nesting boundary condition appears to work very well in this case, by both forcing the NG2 solution to be consistent with the NG1 solution and avoiding spurious reflections at the interface. In the following analysis of the impact of relief on the flow, only results obtained on the high-resolution grid NG2 will be considered.

The vertical profiles of wind speed measured *in situ* and simulated are displayed in Fig. 8, at two different locations: T4 and T1 (see Fig. 5). T1 is located at the bottom of the valley ($z=82$ m), whereas T4 is located on a small plateau dominating the valley ($z=117$ m). Two simultaneous series of measurements (LCPC, permanent tower and Institut National de Recherche Agronomique (INRA), additional tower) are available during the considered period. From the measurements, "LCPC"—the main deformation into the valley—leads to an important decrease in the wind speed of about 1.3 m/s between T4 and T1. The deceleration of the flow into the valley is well reproduced by the model, despite the relatively low vertical resolution close to the ground, which does not allow us to predict the observed strong gradients of wind within the first meters above the ground. Note that at the same time, the wind is deflected to the north in the valley, which is in agreement with measurements.

Therefore, SUBMESO code provides wind field (and air temperature, not shown here because gradients are very weak in these conditions) at each point of its mesh, the first nodes of which are located 5 m above the ground. Wind speed values issued from SUBMESO (three components) are next expressed in terms of horizontal wind speed and direction in order to be adapted to PE calculations. Below 5 m, temperature and wind vertical profiles are assumed to be logarithmically shaped. Thus the refraction parameters $a_T$ and $a_v$ [Eq. (10)] can be fitted using the first point (5 m high) provided by SUBMESO. The corresponding vertical profile of sound speed [Eq. (12)] is assumed to be constant, but can be chosen as representative of the studied source-receiver configuration for medium-range propagation: valley, plateau, downslope, upslope, etc. It must be noticed that since mesh adaptation and data interpolation from SUBMESO to PE is not automatic yet, vertical profiles are still range independent. Further work is currently in progress in order to take into account the "exact" wind and temperature values at each point of the PE grid, directly interpolated from SUBMESO output data, leading to range dependent vertical profiles of sound speed on such irregular terrain.

Thus SUBMESO code provides synthetic *local* (site scale) wind and temperature vertical profiles from input data collected at larger scales (e.g., "Météo-France" national stations). Those large-scale input data can be chosen as average (e.g., a 30 year average) data, leading to SUBMESO output data representative of long-term (e.g., a 30 year average) atmospheric conditions at a local site. Therefore, output data from SUBMESO can be used as input data for the PE code, leading to SPL predictions for various micrometeorological conditions, including site effect (space sensitivity, e.g., topography) *and* long-term mean conditions (time sensitivity, e.g., a 30 year average). Those long-term averages can be chosen either for day, evening night, day and night, etc., periods, or for a more global period of 24 h.

The next part of this study show a comparison between experimental acoustic data extracted from a specific campaign carried out on the LCPC monitoring site located at Saint-Berthevin and MW-WAPE predictions (Fig. 9). During this experimental campaign, acoustic data have been measured for typical atmospheric conditions, i.e., for *local* micrometeorological conditions *directly* collected at the same site *and* at the same time using *synchronized* meteorological sensors from Saint-Berthevin equipped towers. Actually, after a scanning of the micrometeorological data measured during this experimental campaign, we chose a period (sample) which was the most representative of a "long-term" (average) period in terms of meteorological parameters predicted by SUBMESO (Table I—Measurement No. 4). Thus, it became possible to compare PE long-term predictions with the corresponding acoustic experimental data. Figures 9(a) and 9(b) give some examples of such long-term (a 30 year average of 24 h periods) PE predictions for downslope propaga-

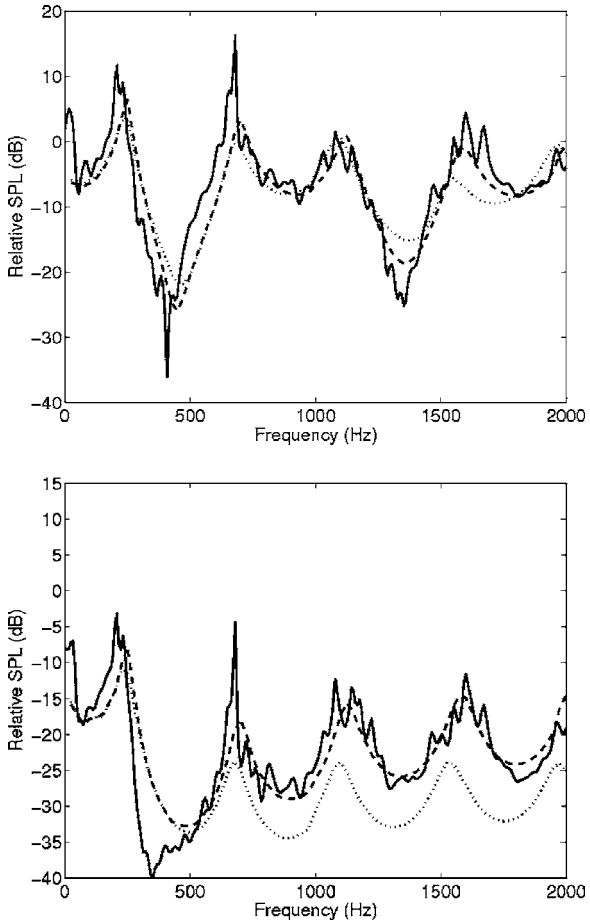


FIG. 9. Examples of results provided by the coupling of the SUBMESO micrometeorological code with the MW-WAPE acoustic code. Relative SPL as a function of frequency: Comparison between experimental results (solid line) and MW-WAPE predictions for long-term (dashed line) and for homogeneous (dotted line) conditions. (a) M1 (25 m) and (b) M4 (75 m).

tion and using the following geometrical parameters values: $h_s=h_M=h_{ref}=2m$. (Table II—Measurement No. 4). Moreover, in order to identify the real effect of long-term average meteorological parameters, we also calculate PE predictions in the same geometric configuration but for homogeneous conditions (dotted line). Micrometeorological parameters are deduced from SUBMESO calculations as presented above. As mentioned above, Figures 9(a) and 9(b) also show acoustic data (solid line) collected during the experimental campaign (Tables I and II—Measurement No. 4), which appear to be very similar to MW-WAPE predictions when considering "long term" atmospheric conditions instead of homogeneous conditions.

The SPL difference between homogeneous and long-term conditions, of course, increases with distance from source, but is already perceptible from medium range propagation [see Fig. 9(b), M4 at 75 m]. This difference can be also quantified, e.g., in one-third octave bands, which can be useful for engineering applications, such as noise impact studies. Figures 9(a) and 9(b) also show that discrepancies between PE predictions and experimental data can be greatly reduced if we can have access to "true" wind and temperature fields on the studied site during the corresponding period. Unfortunately, for engineering or operational situations, such experimental data cannot be always collected due to financial cost and/or *in situ* constraints. This study showed that SUBMESO can provide those wind and temperature profiles at almost any site (local scale), which can be chosen as mean values representative of a chosen period (short term or long term, e.g., 30 years).

Consequently, the MW-WAPE/SUBMESO coupled code can be used for estimating long-term SPL representative of mean (e.g., a 30 year average) atmospheric conditions at a local site, even on irregular terrain. It must be mentioned that this coupling approach do not yet take into account nonlinear effects of both acoustical and micrometeorological models. These first numerical results are presented as a first stage of a research program which is still in progress, and which will be carried out in the next few years, partially based on the exploitation of the database from the LCPC monitoring site located at Saint-Berthevin.

## V. CONCLUSION

This study takes place in the framework of road traffic noise propagation. Our coupling approach gives us access to reliable SPL predictions for a specific source-receiver configuration (local scale) and propagation conditions (long term). This is carried out through the use of reference models for both acoustic (MW-WAPE) and micrometeorological (SUBMESO) calculations, which have been presented, discussed, and validated by comparison with experimental data.

The MW-WAPE code takes into account the convection properties of cross-wind effects on acoustic propagation. Moreover, in spite of some approximations in the ground impedance model, it can deal with realistic environments (uneven ground, impedance jumps, absorbent barriers, etc.) and complex propagation conditions (range dependent refraction profiles and atmospheric turbulence).

The SUBMESO micrometeorological code provides synthetic local (small scale) wind and temperature vertical profiles from global ones (regional scale). For the input profiles to the SUBMESO code, one can use long-term average atmospheric averages. In our study, we used 30 year averages, which for practical purposes can be interpreted as long-term averages. Then, output data from SUBMESO have been used as micrometeorological input data for MW-WAPE calculations between the source and receiver, in order to calculate SPL representative of *local* and *long-term* atmospheric conditions between the source and receiver. Examples of MW-WAPE/SUBMESO coupling have been presented and discussed. They can be considered as very promising results regarding both the complementary nature and the reliability of the coupled models, although some refinements still should be done on the automatic coupling procedure. Currently, further research is in progress in order to take into account range dependent profiles, line sources, 3D and nonlinear effects, and various propagation conditions.

## ACKNOWLEDGMENTS

The authors are very grateful to Keith Wilson (Associate Editor) and reviewers for their insightful comments that have led to the improvement of this manuscript.

[1]Embleton, T. F. W., "Tutorial on sound propagation outdoors," J. Acoust. Soc. Am. **100**, 31–48 (1996).
[2]Heimann, D., and Gross, G., "Coupled simulation of meteorological parameters and sound level in a narrow valley," Appl. Acoust. **56**, 73–100 (1999).
[3]Hole, L. R., and Hauge, G., "Simulation of a morning air temperature inversion break-up in complex terrain and the influence on sound propagation on a local scale," Appl. Acoust. **64**, 401–414 (2003).
[4]Blumrich, R., and Heimann, D., "A linearized Eulerian sound propagation model for studies of complex meteorological effects," J. Acoust. Soc. Am. **112**, 446–455 (2002).
[5]Ostashev, V. E., Wilson, D. K., Liu, L., Aldridge, D. F., Symons, N. P., and Martin, D., "Equations for finite-difference, time-domain simulation of sound propagation in moving inhomogeneous media and numerical implementations," J. Acoust. Soc. Am. **117**, 503–517 (2005).
[6]Salomons, E. M., Blumrich, R., and Heimann, D., "Eulerian time-domain model for sound propagation over a finite-impedance ground surface. Comparison with frequency-domain models," Acta. Acust. Acust. **88**, 483–492 (2002).
[7]Craddock, J. M., and White, M. J., "Sound propagation over a surface with varying impedance: A parabolic equation approach," J. Acoust. Soc. Am. **91**, 3184–3191 (1992).
[8]Rasmussen, K. B., and Galindo Arranz, M., "The insertion loss of screens under the influence of wind," J. Acoust. Soc. Am. **104**, 2692–2698 (1998).
[9]Galindo, M., "Approximations in the PE method. Phase and level errors in a downward refracting atmosphere," *Int. Symp. on Long Range Sound Propagation*, Lyon, France, 235–255 (1996).
[10]Salomons, E. M., "Diffraction by a screen in downwind sound propagation: A parabolic equation approach," J. Acoust. Soc. Am. **95**, 3109–3117 (1994).
[11]Blairon, N., Blanc-Benon, P., Bérengier, M., and Juvé, D., "Calculation of sound propagation over uneven terrain using parabolic equation," Invited Paper to 17th ICA, Proceedings Volume III, CD-Rom ISBN 88-88387-02-1, Rome (2001).
[12]Blairon, N., Blanc-Benon, P., Bérengier, M., and Juvé, D., "Outdoor sound propagation in complex environment: experimental validation of a PE approach," *10th Int. Symp. on Long Range Sound Propagation*, Grenoble, France, 114–128 (2002).
[13]Blairon, N., "Topography effect on acoustic propagation in the atmosphere: Numerical modelization using parabolic equation and validation by comparison with outdoor experiments," (in French) Ph. D. thesis, École Centrale de Lyon, France (2002).
[14]Gauvreau, B., Bérengier, M., Blanc-Benon, P., and Depollier, C., "Traffic noise prediction with the parabolic method: Validation, of a split-step Padé approach in complex environments," J. Acoust. Soc. Am. **112**, 2680–2687 (2002).
[15]Blanc-Benon, P., Lihoreau, B., Pénelon, T., Gauvreau, B., Calmet, I., and Bérengier, M., "Outdoor sound propagation in complex environments using the parabolic equation: A new PE code coupled with a micrometeorological code," *11th Int. Symp. on Long Range Sound Propagation*, Lake Morey, USA (2004).
[16]Xue, M., Droegemeier, K. K., and Wong, V., "The advanced regional prediction system (ARPS)—A multiscale nonhydrostatic atmospheric simulation and prediction model. Part I: Model dynamics and verification," Meteorology and Atmos. Phys. **75**, 161–193 (2000).
[17]Godin, O. A., "Wide-angle parabolic equation for sound in 3D inhomogeneous moving medium," Dokl. Phys. **47**, 643–646 (2002).
[18]Lingevitch, J. F., Collins, M. D., Dacol, D. K., and Drob, D. P., "A wide angle and high Mach number parabolic equation," J. Acoust. Soc. Am. **111**, 729–734 (2002).
[19]Blanc-Benon, P., Dallois, L., and Juvé, D., "Long-range sound propagation in a turbulent atmosphere within parabolic equation," Acta. Acust. Acust. **87**, 659–669 (2001).
[20]Ostashev, V. E., Juvé, D., and Blanc-Benon, P., "Derivation of a wide-angle parabolic equation for sound waves in inhomogeneous moving media," Acta. Acust. Acust. **83**, 455–460 (1997).
[21]Dallois, L., Blanc-Benon, P., and Juvé, D., "A wide-angle parabolic equation for acoustic waves in homogeneous moving media: Application to atmospheric sound propagation," J. Comput. Acoust. **9**, 477–494 (2001).
[22]Delany, M. E., and Bazley, E. N., "Acoustical properties of fibrous absorbent materials," Appl. Acoust. **3**, 105–116 (1970).
[23]Panofsky, H. A., and Dutton, J. A., *Atmospheric Turbulence* (Wiley, New York, 1984).
[24]Gilbert, K. E., and White, M. J., "Application of the parabolic equation to sound propagation in a refracting atmosphere," J. Acoust. Soc. Am. **85**, 630–637 (1989).
[25]Juvé, D., Blanc-Benon, P., and Chevret, P., "Numerical simulation of sound propagation through a turbulent atmosphere," *Proceedings of the 5th Int. Symp. on Long Range Sound Propagation*, Milton Keynes, UK 282–286 (1992).
[26]Klemp, J. B., and Wilhelmson, R. B., "The simulation of three-dimensional convective storm dynamics," J. Atmos. Sci. **35**, 1070–1096 (1978).
[27]Smagorinsky, J., "General circulation experiments with the primitive equations: I,"Mon. Weather Rev. **91**, 99–164 (1963).
[28]Lilly, J. B., "The representation of small-scale turbulence in numerical simulation experiments," *Proc. IBM Sci. Comput. Symp. on Env. Sci., N. Y.*, IBM Form 3201951, 195–210 (1967).
[29]Blayo, E., and Debreu, L., "Adaptive mesh refinement for finite-difference ocean models: First experiments," J. Phys. Oceanogr. **29**, 1239–1250 (1999).
[30]Pénelon, T., "Meteorological simulations of a rural site with a nonplan topography using the nesting technique with SUBMESO," (in French), Ph.D thesis, École Centrale de Nantes – Université de Nantes, France (2002).
[31]Carpenter, K. M., "Note on the paper: Radiation conditions for the lateral boundaries of limited-area numerical models by M. J. Miller and A. J. Thorpe (Q.J., 107, 605–628)," Q. J. R. Meteorol. Soc. **108**, 717–719 (1982).
[32]Chen, C., "A nested grid, nonhydrostatic, elastic model using a terrain-following coordinate transformation: The radiative-nesting boundary conditions," Mon. Weather Rev. **119**, 2852–2869 (1991).
[33]DeCroix, D. S., "Large-eddy simulations of convective and evening transition planetary boundary layers," Ph. D. thesis, Department of MEAS, NCSU, USA (2001).
[34]Bérengier, M., and Garai, M., "A state-of-the-art of in situ measurement of the sound absorption coefficient of road pavements," *17th Int. Cong. Acous.*, Rome, Italy (2001).
[35]Legeay, V., and Seznec, R., "On the determination of acoustic characteristics of absorbent materials," (in French), Acustica **53**, 171–192 (1983).
[36]Attenborough, K., "Acoustical impedance models for outdoor ground surface," J. Sound Vib. **99**, 521–544 (1985).
[37]Daigle, G. A., "Effects of atmospheric turbulence on the interference of sound waves near a hard boundary," J. Acoust. Soc. Am. **64**, 622–630 (1978).
[38]Daigle, G. A., "Effects of atmospheric turbulence on the interference of sound waves above a finite impedance boundary," J. Acoust. Soc. Am. **65**, 45–49 (1979).
[39]Chevret, P., Blanc-Benon, P., and Juvé, D., "A numerical model for sound propagation through a turbulent atmosphere near the ground," J. Acoust. Soc. Am. **100**, 3587–3599 (1996).
[40]Wilson, D. K., Brasseur, J. G., and Gilbert, K. E., "Acoustic scattering and the spectrum of atmospheric turbulence," J. Acoust. Soc. Am. **105**, 30–34 (1999).
[41]Karweit, M., Blanc-Benon, P., Juvé, D., and Comte-Bellot, G., "Simulation of the propagation of an acoustic wave through a turbulent velocity field: A study of phase variance," J. Acoust. Soc. Am. **89**, 52–62 (1991).